

# Effective and efficient transport mechanism of CO<sub>2</sub> in subnano-porous crystalline membrane of syndiotactic polystyrene

Yoshinori Tamai\*

*Department of Applied Physics, Faculty of Engineering, University of Fukui, 3-9-1 Bunkyo, Fukui 910-8507, Japan*

---

## Abstract

The gas permeation behavior in the single crystal of syndiotactic polystyrene (s-PS) S-I form was investigated in detail, in comparison to that in the s-PS  $\epsilon$  form. The S-I form exhibits high separation factors for CO<sub>2</sub>/N<sub>2</sub> ( $\sim 180$ ) and CO<sub>2</sub>/CH<sub>4</sub> ( $\sim 500$ ), while preserving its high CO<sub>2</sub> permeability 8000 Barrers; a trade-off between selectivity and permeability was broken through. The mechanism of the effective and efficient transport of CO<sub>2</sub> in the S-I form was examined in relation to the cavity structure in the crystal. Because the CO<sub>2</sub> molecule is only fitted to the cavities in the S-I form, the solubility of CO<sub>2</sub> becomes high. In addition, it was found that tri-atomic molecules can more effectively diffuse in the S-I form compared with di-atomic molecules. This peculiar behavior, larger molecule can diffuse more quickly, was proved by using a “long-gas” model, in which long-axis lengths of N<sub>2</sub> and O<sub>2</sub> were extended to that of CO<sub>2</sub>. A novel design criterion for the CO<sub>2</sub> separation membranes is proposed based on the aspect of momentum transfer from polymer matrix to the penetrant, whose re-orientational motion is coupled to jump trials between cavities.

*Keywords:* gas separation, molecular dynamics simulation, polystyrene, crystal, stress

---

## 1. Introduction

Membrane separation is expected to be widely used because it is an energy saving and maintenance free process. To install the membrane separation system in large-scale plants, such as carbon capture in power plants or natural gas fields, both selectivity and permeability should be raised. However, as argued by Robeson [1] and reviewed by Park et. al [2], there is a trade-off between permeability and selectivity. In the plot of selectivity vs. permeability (so-called Robeson plot), an upper bound is drawn as a linear declined line. Many

---

\*Corresponding author

*Email address:* tamai@u-fukui.ac.jp (Yoshinori Tamai)

efforts have been made to overcome the upper bound [2].

To raise both of the competing properties, selectivity and permeability, we attempt to apply a “molecular cavity” to porous polymer crystal [3]. The molecular cavity is a small vacant space in crystals, in which a guest molecule can be just fitted. The cavity is characterized by regular size, regular shape, and ordered connectivity. The permeability of gases in the molecular cavity may be controlled by external stimulus. For example, by applying stress to the porous crystal, the connectivity of molecular cavities may be changed and the size and connectivity of permeation channels may be controlled; penetrants are precisely separated by size, and only particular species can be effectively permeated.

The use of ordered structures to the separation processes is familiar in the field of inorganic membrane, such as zeolites [4, 5], graphene [6, 7], and various nano-sheets [8, 9]. One of the advantages of using porous polymer crystals is that the main chains are rather flexible. Local segmental motion of the chains may help the transport of gas molecules.

Some crystalline forms of syndiotactic polystyrene (s-PS) are expected to be candidates to realize the concept of the molecular cavity, because of their porous nature [10, 11]. As reviewed by some authors [10–12], s-PS is known for complex polymorphic behavior. There are five main polymorphs:  $\alpha$  [13–16],  $\beta$  [17, 18],  $\gamma$  [19–22],  $\delta$  [23–26], and  $\varepsilon$  [27, 28] form. The  $\delta$  and  $\varepsilon$  forms have porous nature; various guest molecules are clathrated in these forms [29–31]. The re-orientational dynamics of guests are significantly affected by host–guest interaction, depending on the guest structure and cavity shape [32–34]. The diffusion of small molecules in these crystals is anisotropic, reflecting crystalline orientations [3, 35, 36]. Narrow channels are also exist in the  $\alpha$  form, in which gas molecules are permeable [37–39], while more dense  $\beta$  form is impermeable to small gas molecules [38]. The diffusion coefficients of gases in the porous  $\delta$  form are about two order of magnitude lower than that in the amorphous phase [40], because each cavity is separated in this form.

These crystalline forms are interchangeable with each other by thermal or solvent treatments [12]. External stresses affect the transition [41–43]. The polymorphic behavior of s-PS were investigated also by atomistic molecular dynamics (MD) simulations [21, 22, 44–46] and coarse-grained simulations [45, 46].

Recently, the author found remarkable structural transition behavior of a subnano-porous crystal of s-PS by using a molecular dynamics (MD) simulation [47]. A new transition path,  $\varepsilon \rightarrow \text{S-I} \rightarrow \gamma$  form, by a uniaxial stress treatment was found, where the S-I form (1st form under stress) was only stable under the stress. The initial and end points,  $\varepsilon$  and  $\gamma$  forms, respectively, are experimentally known forms, while the S-I is a newly found form. The rearrangement of nano-porous cavity structures associated with stress-induced phase transitions was also reported [47]. It was demonstrated that the nano-scale channel in the  $\varepsilon$  form was transformed into a zigzag

channel suitable for gas separations. From preliminary simulations [48], the permeability of gases in the S-I form exhibited the possibility of effective CO<sub>2</sub>/N<sub>2</sub> and CO<sub>2</sub>/CH<sub>4</sub> separation.

The reproducibility of the transition and stability of the S-I form were thoroughly confirmed in a previous study [44]. Various thermal and stress induced transitions of s-PS were examined in the wide range of temperature–stress plane and a kind of phase diagram was derived. It was found that the S-I form was more stable than the  $\delta_e$  and  $\epsilon$  forms and most stable under the stress of  $\sigma_{yy} = 0.27$  GPa at 300 K.

In the present paper, the S-I crystal structure is fully characterized for the first time, using the atom coordinates obtained in the previous study [44]; the fractional coordinates of atoms in an asymmetric unit were determined. The main objective of the present paper is investigating permeation behaviors of gas molecules in the newly determined S-I form crystal by MD simulations. The solubilities and diffusion constants of gases, H<sub>2</sub>, O<sub>2</sub>, N<sub>2</sub>, CH<sub>4</sub>, and CO<sub>2</sub>, in the S-I form are examined by long-time MD simulations, compared with those in the  $\epsilon$  form. It is shown that the S-I form exhibits extremely high CO<sub>2</sub>/N<sub>2</sub> and CO<sub>2</sub>/CH<sub>4</sub> selectivity while preserving its high CO<sub>2</sub> permeability. A noteworthy finding is that tri-atomic molecules can more effectively diffuse in the S-I form compared with di-atomic molecules. In other words, a larger molecule can diffuse more quickly. In order to clarify the mechanism of this peculiar behavior, further MD simulations are performed using a “long-gas” model, in which long-axis length of N<sub>2</sub> and O<sub>2</sub> is extended to that of CO<sub>2</sub>. The results are interpreted in terms of effective momentum transfer from the polymer matrix to the penetrants.

## 2. Simulation details

### 2.1. Force field

The force field for s-PS, AMBER [49], was the same as those used previously [22, 44, 47]. The applicability of the force field was confirmed in the previous papers. The partial charges were assigned only for aromatic hydrogens (+0.085e) and aromatic carbons bonded to the hydrogen (−0.085e). Using the model, experimentally determined crystal structures of s-PS polymorphs were satisfactorily reproduced. Various transition paths among these polymorphs by temperature or stress treatments were also reproduced by the model [22, 44].

The force-field parameters for gas molecules are listed in Table 1, where  $\sigma_{LJ}$  and  $\epsilon_{LJ}$  are the size and energy parameters, respectively, of 12–6 Lennard-Jones (LJ) potential and  $q$  is the partial charge. The CO<sub>2</sub>, N<sub>2</sub>, O<sub>2</sub>, and H<sub>2</sub> molecules were modeled as rigid body with quadrupole. The quadrupole moments were modeled by three partial charges; an additional interaction site, M, was introduced at the center of each diatomic molecule. The transferable potential for phase equilibria (TraPPE) force field developed by Potoff and Siepmann [50]

Table 1: Force-field parameters for gases [50–53].

gas	atom <sup>a</sup>	$\sigma_{\text{LJ}}$ (Å)	$\varepsilon_{\text{LJ}}$ (kJ/mol)	$q$ (e)	$l_{\text{b}}$ <sup>b</sup> (Å)
CO <sub>2</sub>	O	3.05	0.657	-0.35	1.16
	C	2.80	0.224	+0.70	
N <sub>2</sub>	N	3.31	0.299	-0.482	0.55
	M	0	0	+0.964	
O <sub>2</sub>	O	3.013	0.408	-0.123	0.605
	M	0	0	+0.246	
H <sub>2</sub>	H	0	0	+0.468	0.37
	M	2.958	0.305	-0.936	
CH <sub>4</sub>	H	2.50	0.126	+0.060	1.09
	C	3.50	0.276	-0.240	

<sup>a</sup>M is massless point to reproduce quadrupole.

<sup>b</sup>Bond length to the center of mass of molecule.

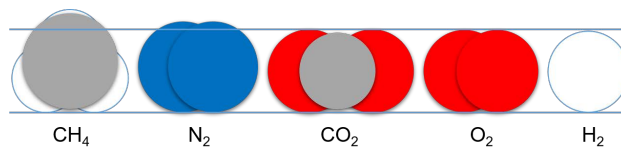


Figure 1: Schematic representation of gas models, based on  $l_{\text{b}}$  and  $\sigma_{\text{LJ}}$ .

was used for CO<sub>2</sub> and N<sub>2</sub>. The model can quantitatively reproduce the vapor-liquid equilibria of neat N<sub>2</sub> and CO<sub>2</sub> and also their mixtures with alkanes [50]. The TraPPE force field with quadrupole was also used for O<sub>2</sub> [51]. The model by Yang et al.[52] was used for H<sub>2</sub>, in which a single LJ site was located between two H atoms and three partial charges were settled on the molecule. OPLS-AA [53] was used for CH<sub>4</sub>. The schematic representation of gas models are shown in Fig. 1, in which sphere size reflects the LJ size parameter  $\sigma_{\text{LJ}}$ .

These gas models have been used extensively in combination with other force fields such as AMBER, OPLS-AA, etc. to investigate gas permeation behavior through membranes. For example, the TraPPE was used to simulate permeation behavior of CO<sub>2</sub> and N<sub>2</sub> through graphene membranes [6, 7], in combination with AMBER

and OPLS-AA force fields. The model of Yang et al. was used to simulate adsorption of CO<sub>2</sub>/CH<sub>4</sub>/H<sub>2</sub> mixture in metal–organic frameworks (MOFs) [52], associated with TraPPE and OPLS-AA.

In our previous study [3, 39, 54], sorption and diffusion of CO<sub>2</sub>, O<sub>2</sub>, and N<sub>2</sub> in s-PS  $\alpha$  and  $\delta_e$  forms have been investigated by other classical gas models: MSM for CO<sub>2</sub> [55] and two center LJ model (without quadrupole) for O<sub>2</sub> and N<sub>2</sub> [56, 57]. The s-PS chains were modeled by AMBER, the same model as in the present study. The same set of force fields was also applied for CO<sub>2</sub> sorption in the  $\delta_e$  form by other authors [58]; the sorption isotherms of CO<sub>2</sub> were successfully reproduced.

To confirm the sensitivity of the force fields on gas permeation behavior, I have also performed gas-permeation simulation in the s-PS S-I and  $\varepsilon$  forms using the latter set of the force fields in addition to the parameter set tabulated in Table 1. The results are summarized in Tables S2–S5 of Supporting Information. It was found that conclusions of the present paper were not affected by the force fields used. From these reasons, the use of the present force field (Table 1) is justified.

### 2.2. Molecular dynamics simulation

The method of MD simulation was the same as those used previously [22, 44, 47]. Three-dimensional periodic boundary condition (PBC) was applied, i.e., infinitely spread single crystals were simulated. Each polymer chain was connected infinitely by the PBC. The LJ interaction was smoothly cut off at 12 Å with a long range correction. The long-range Coulomb interactions were handled by the Ewald sum method. The Nosé [59] method was used to control temperature (300 K) and the Parrinello–Rahman [60] method was used to control the pressure tensor of the system. All the bond lengths of polymer and CH<sub>4</sub> were constrained by the SHAKE method [61]. The other gas molecules were treated as rigid body by the SHAKE vectorial constraint method [61, 62]. The equations of motion were solved by a variant of the Verlet algorithm [63, 64], with a time step of 1 fs. Although no constraint forces to keep the center of mass (COM) of whole crystal were applied, drifts of the COM were negligible.

### 2.3. Crystal-structure determination

The s-PS S-I form was obtained in the previous study, in which the initial  $\varepsilon$  form crystal was transformed into the S-I form by stress treatment [44]. Specifically, a uniaxial stress along the  $b$ -axis was gradually applied to the crystal by changing the  $yy$  component of the symmetric tensor  $\Sigma$  stepwise at a rate of 1 kJ/molÅ per 130 ps. The symmetric tensor  $\Sigma$  of the Parrinello–Rahman method [60] is related to the external stress  $\sigma$  as:

$$\Sigma = \mathbf{h}_0^{-1}(\sigma - p)(\mathbf{h}_0^{-1})^t V_0, \quad (1)$$

where  $\mathbf{h}$  is the cell matrix,  $p$  is hydrostatic pressure,  $V$  is the volume of the MD unit cell, and the subscript 0 denotes the reference state. Starting from the  $\varepsilon$  form with  $3 \times 2 \times 6$  crystal units the structural transition to the S-I form was initiated at  $\Sigma_{yy} = 16$  kJ/molÅ (at 300 K), which corresponded to a stress of  $\sigma_{yy} = 0.43$  GPa. The stress was released to 0.27 GPa through the structural transition. After further compression to  $\Sigma_{yy} = 25$  kJ/molÅ ( $\sigma_{yy} = 0.41$  GPa), the stress was gradually reduced to  $\Sigma_{yy} = 15$  kJ/molÅ ( $\sigma_{yy} = 0.27$  GPa). In the previous study [44], the thermal stability of the S-I form was examined under various  $\Sigma_{yy}$  values. Because the S-I form was found to be the most stable under a stress of  $\sigma_{yy} = 0.27$  GPa, that structure was examined in this study.

The structure factor  $F_{hkl}$  and X-ray intensity  $I_{hkl}$  for the Miller index ( $hkl$ ) was calculated by a procedure shown in Appendix A. The intensity  $I_{2\theta}$  for diffraction angle  $2\theta$  was calculated by summing  $I_{hkl}$  values for ( $hkl$ )s that are related to the same  $2\theta$  within a small tolerance. The  $F_{hkl}$ ,  $I_{hkl}$ , and  $I_{2\theta}$  values were averaged over 200 configurations during 100 ps. The crystal space group was determined by examining the deduction of  $F_{hkl}$  for particular sets of  $hkl$ .

The fractional coordinates of atoms were calculated for each coordinate every 500 steps (0.5 ps), and averaged over 100 ps trajectories. The averages were also taken over all 72 crystal units in the S-I MD unit cell. The coordinates of an asymmetric unit were selected from the averaged coordinates of eight monomer units.

#### 2.4. Simulation of gas permeation

The S-I crystal model consisted of  $4 \times 3 \times 6$  crystal units was generated using the determined space group information and coordinates of the asymmetric unit. In this MD unit cell setting,  $\Sigma_{yy}$  is equal to 7 kJ/molÅ (instead of  $\Sigma_{yy} = 15$  kJ/molÅ) to conform  $\sigma_{yy} = 0.27$  GPa. The condition is different from that used in the preliminary calculation [48], where  $\sigma_{yy} = 0.18$  GPa using the MD unit cell with  $6 \times 2 \times 6$  crystal units. The structure of the  $\varepsilon$  form consisted of  $3 \times 2 \times 6$  crystal units was generated based on the experimentally determined structure [28]. The crystals were equilibrated for 200 ps at 300 K.

The excess chemical potential  $\mu_r$  of gas molecule in the crystal was calculated by the Widom particle insertion method [65] as

$$\mu_r = -k_B T \ln \langle \exp(-u/k_B T) \rangle, \quad (2)$$

where  $u$  is energy difference before and after insertion of a test molecule,  $k_B$  is Boltzmann constant,  $T$  is temperature, and  $\langle \dots \rangle$  means ensemble average. 100,000 insertion trials of the test molecule were attempted to each of 200 configurations during 100 ps. The excluded volume map sampling (EVMS) was used to raise the

efficiency of sampling [66]. To estimate the standard error, sampling points were divided into 40 subsets, each of which consists of 5 configurations. The solubility  $S$  was calculated by

$$S = \exp(-\mu_r/k_B T), \quad (3)$$

whose unit was translated into  $\text{cm}^3(\text{STP})/\text{cm}^3\text{atm}$  by multiplying  $273.15/T$ , where  $T$  is temperature in K (300 K).

In order to simulate the diffusion behavior, gas molecules were inserted into the crystal, such that only one molecule diffuse in each separated channel. A total of 24 and 12 molecules were inserted in the S-I and  $\varepsilon$  form, respectively. The simulation runs of 10 ns were performed separately for five gas species,  $\text{H}_2$ ,  $\text{O}_2$ ,  $\text{N}_2$ ,  $\text{CH}_4$ , and  $\text{CO}_2$ , at 300 K. The simulations of gas diffusion were repeated for three times for each system and obtained physical quantities were averaged over three runs.

All simulation runs and numerical analyses were performed with the PAMPS [67] molecular simulation program coded by the author, using the super computer at ACCMS, Kyoto University.

### 3. Results and discussion

#### 3.1. Crystal structure of S-I form

A snapshot of the S-I and  $\varepsilon$  forms are shown in the previous paper [44]. The crystal system of these forms is orthorhombic. The symmetry of the crystal was changed by the structural transition, and one crystal unit of the  $\varepsilon$  form was separated into two units in the S-I form. In the crystal unit, there are eight monomer units (two helices) in the S-I form, whereas there are sixteen monomer units (four helices) in the  $\varepsilon$  form. A crystal unit of the S-I form under  $\sigma_{yy} = 0.27$  GPa stress is depicted in Fig. 2. One right-handed (R, blue) and one left-handed (L, red) helix are contained in a unit cell. Some monomer units are translationally duplicated for better visualization. The crystal lattice parameters of the S-I form are listed in Table 2, compared to the other forms. Note that the lattice parameters  $a$  and  $b$  vary with external stress  $\sigma_{yy}$ ; the values of  $a$  and  $b$  are reduced or enlarged, respectively, with decreasing  $\sigma_{yy}$ . The S-I form can exist above  $\sigma_{yy} = 0.04$  GPa in the condition of the previous study [44], including a metastable state. The density of the S-I form,  $0.969 \text{ g/cm}^3$ , is approximately the same as that of the empty  $\delta_e$  form.

The calculated structure factors and X-ray diffraction intensities are listed in Table S1 of Supporting Information. The intensities are also plotted *vs.*  $2\theta$  in Fig. S1 of Supporting Information. The most significant peak for the S-I form is around  $2\theta = 14.9^\circ$ , which is attributed to the  $\{111\}$  plane. The peak around  $2\theta = 8^\circ$

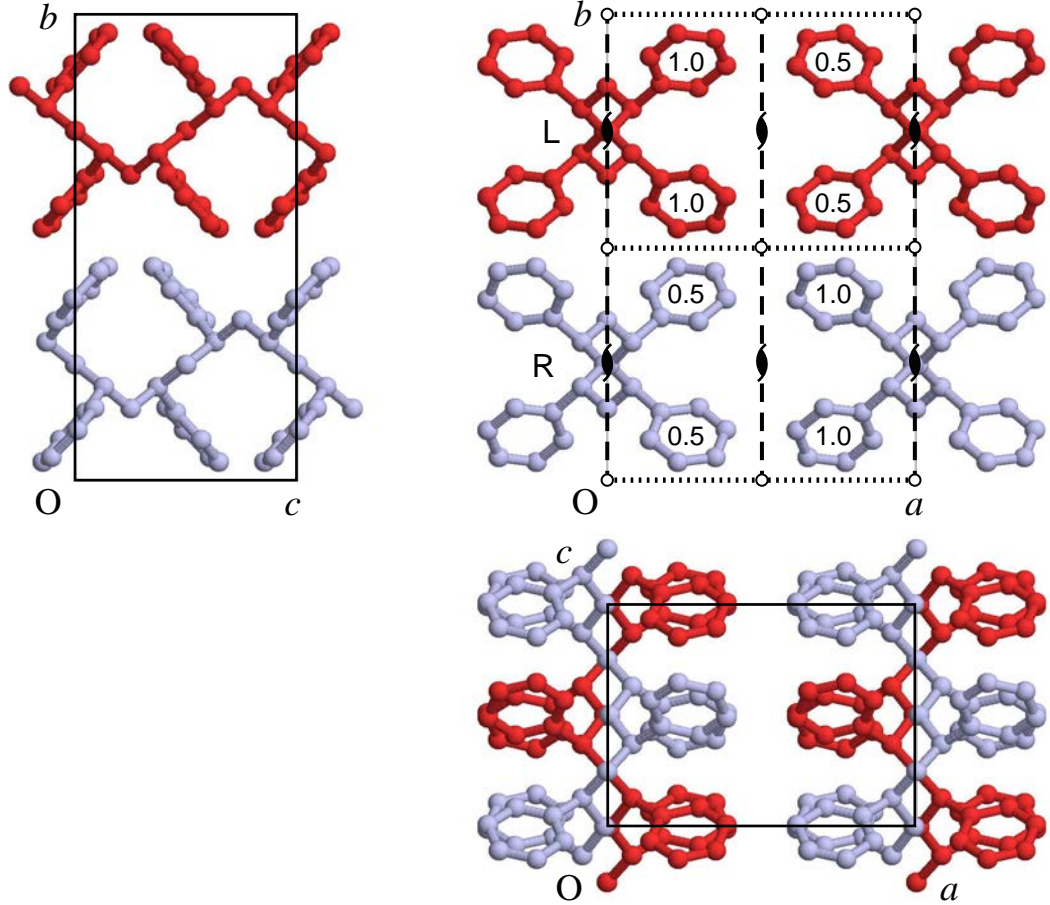


Figure 2: Snapshots of a s-PS S-I form crystal under the stress of  $\sigma_{yy} = 0.27$  GPa. The right-handed (R) and left-handed (L) helices are light blue and red, respectively. The approximate fractional coordinates  $z/c$  of the barycenters of the phenyl rings are shown.

is from the (100) plane; the Bragg distance  $d = 10.96$  Å agrees well with the  $a$ -length. Systematic absences of  $00l$  and  $h0l$  reflections with  $l = 2n + 1$ , and absences of  $0k0$ ,  $hk0$ , and  $0kl$  reflections with  $k = 2n + 1$ , were found. Those intensities had less than 1 ppm of the maximum diffraction intensity. Because these observations are characteristic of the space group  $Pbc\bar{b}$  (No. 54) [68], the space group of the S-I form was determined as  $Pbc\bar{b}$ . The space group can be transformed into  $Pcaa$  by changing the cell setting to  $\mathbf{abc} \rightarrow \mathbf{ba}\bar{c}$ .  $Pcaa$  is the same space group as that of other helical syndiotactic polymers, such as the clathrate form of syndiotactic

Table 2: Lattice constants of s-PS crystalline polymorphs.

form	space group	$a$ (Å)	$b$ (Å)	$c$ (Å)	$\gamma$ (deg.)	$\rho$ (g/cm <sup>3</sup> )
S-I <sup>a</sup>	<i>Pbcb</i>	10.96	16.55	7.87	90	0.969
$\varepsilon$ <sup>b</sup>	<i>Pbcn</i>	16.1	21.8	7.9	90	0.98
$\gamma$ -I <sup>c</sup>	<i>P2<sub>1</sub>/a</i>	19.42	8.52	7.93	83.4	1.061
$\gamma$ -II <sup>c</sup>	<i>I2</i>	19.37	17.26	7.76	96.4	1.073
$\delta_e$ <sup>d</sup>	<i>P2<sub>1</sub>/a</i>	17.4	11.85	7.70	117	0.977

<sup>a</sup>This work, under stress of  $\sigma_{yy} = 0.27$  GPa.

<sup>b</sup>Petraccone et al. [28]

<sup>c</sup>Simulation by Tamai [22].

<sup>d</sup>De Rosa et al. [26], empty form.

Table 3: Fractional atomic coordinates for an asymmetric unit of the s-PS S-I form for the space group *Pbcb*.

atom <sup>a</sup>	$x/a$	$y/b$	$z/c$	occupancy
C1	0.008	0.250	0.500	0.5
C2	0.000	0.345	0.750	0.5
C <sub><math>\alpha</math></sub>	0.081	0.298	0.629	1
C <sub>A</sub> 1	0.175	0.352	0.548	1
C <sub>A</sub> 2	0.141	0.411	0.432	1
C <sub>A</sub> 3	0.228	0.459	0.354	1
C <sub>A</sub> 4	0.350	0.449	0.393	1
C <sub>A</sub> 5	0.385	0.391	0.509	1
C <sub>A</sub> 6	0.297	0.343	0.587	1

<sup>a</sup>C1, C2: methylene carbon, C <sub>$\alpha$</sub> :  $\alpha$  carbon, C<sub>A</sub>: aromatic carbon.

poly(*m*-methylstyrene) (s-PMMS) containing CS<sub>2</sub> [69].

The fractional coordinates of atoms of an asymmetric unit of the S-I form are listed in Table 3. One monomer unit plus one main-chain carbon atom constitute the asymmetric unit. Note that the occupancy factor is 0.5 for the two main-chain carbons C1 and C2 (other than the  $\alpha$ -carbon). Fig. 2 was drawn based on these

fractional coordinates and the transformation matrices according to the space group  $Pbc2_1$ . Graphical symbols for the symmetry elements [68] are also given. The main-chain C1 resides approximately on the two-fold screw axis. There is an 'axial' glide plane (indicated by dashed lines) along the  $b$ -axis, which is a combination of  $\mathbf{b}/2$  translation and mirror operation by the plane. The L helix (red) can be generated from the R helix (blue) by this symmetry operation.

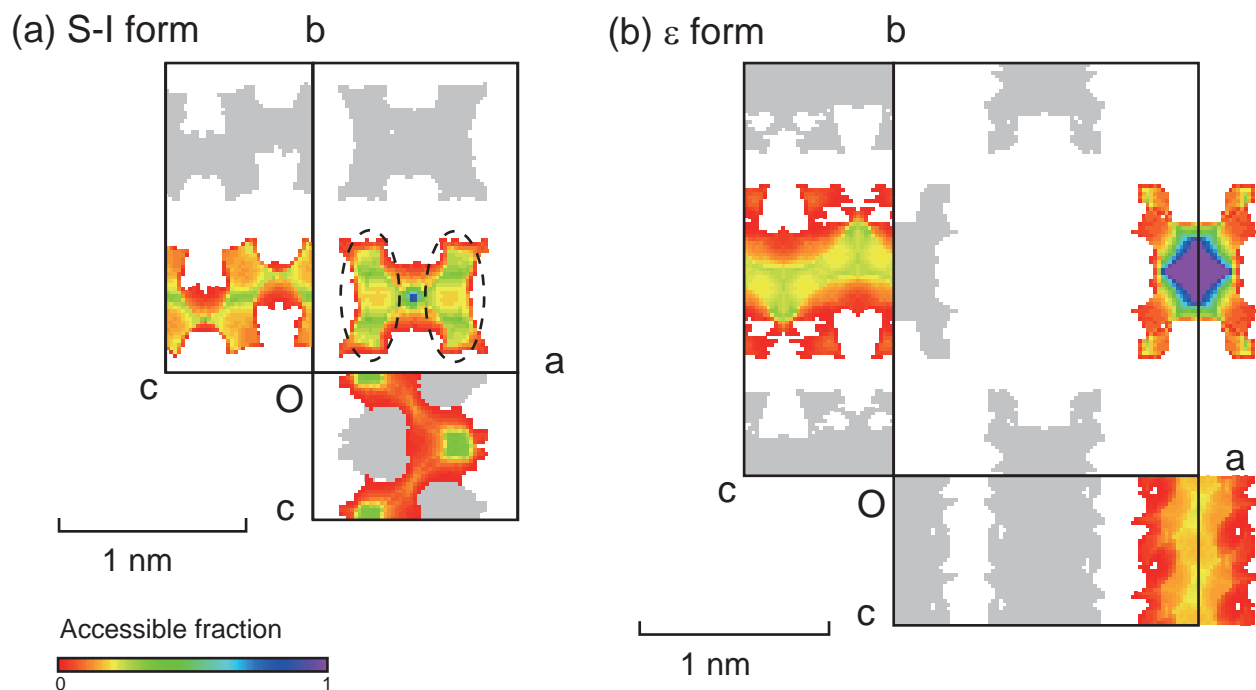


Figure 3: Accessible volume cluster for a probe of radius  $0.7 \text{ \AA}$  in static structure of a crystal unit cell, viewed in  $a$ - $b$ ,  $b$ - $c$ , and  $c$ - $a$  planes. Only one continuous cluster is colored for each form for clarity. The color scale shows accessible fraction along the normal axis to the plane; "1" means completely accessible along the normal axis, i.e., a straight channel exists. Small ellipsoidal cavities in the S-I form were indicated by dashed lines.

### 3.2. Cavity structure

The free volume clusters in the S-I and  $\epsilon$  forms were analyzed. The cell was divided into a three-dimensional grid with an interval of  $0.2 \text{ \AA}$  and the grid points accessible for spherical probes of radius  $R$  were extracted. A cluster analysis [66] was also performed for the accessible grid points.

Fig. 3 shows the accessible volume cluster for a probe of  $R = 0.7 \text{ \AA}$ , calculated for the static (initial or experimental) structure of a crystal unit cell. Only one continuous cluster is drawn for each crystal cell. The size and position of the cavities reflect the chain arrangements and contacts. In the  $\varepsilon$  form, wide tube-like channels along the  $c$ -axis appear. It is known that large solvent molecules, such as  $n$ -octane, can be hosted in the  $\varepsilon$  form [30].

In the S-I form, on the other hand, smaller cavities, indicated by dashed ellipse in the figure, are alternatively connected by narrow channels; zigzag channels along the  $c$ -axis are formed. It is expected that the  $\text{CO}_2$  molecule is just fitted in the small cavities of the S-I form.

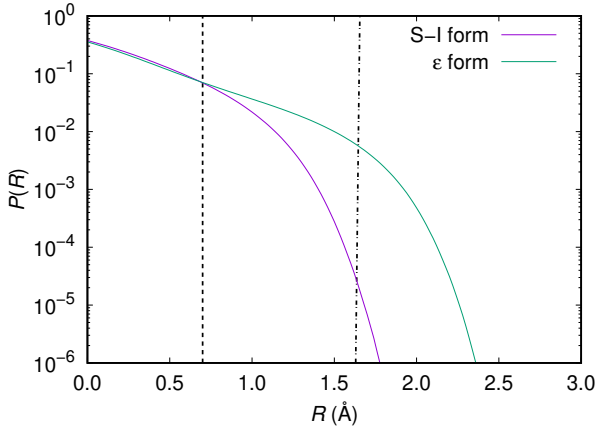


Figure 4: Accessible volume fraction  $P(R)$  for probes of radius  $R$  in the S-I and  $\varepsilon$  forms at 300 K. The vertical dashed line at  $R = 0.7 \text{ \AA}$  indicates the probe radius used for cluster analysis in Fig. 3. The position of  $R = 1.655 \text{ \AA}$ , which is the half of  $\sigma_{\text{LJ}}$  of nitrogen atom, is also shown by dash-dotted line.

Figure 4 shows the  $R$  dependency of the accessible volume fraction  $P(R)$  in the S-I and  $\varepsilon$  forms. The position of  $R = 0.7 \text{ \AA}$  is shown by vertical dashed line. The effects of thermal fluctuation of the polymer chains are naturally incorporated because the distribution was averaged over 200 configurations during 100 ps of MD simulation at 300 K. The radius of nitrogen atom in  $\text{N}_2$ , which is estimated as half value of  $\sigma_{\text{LJ}}$  for N, is shown by vertical dash-dotted line, where the accessible volume for nitrogen atom is more than two order higher in the  $\varepsilon$  form than in the S-I form. The  $P(R)$  distribution is extended to larger  $R$  for the  $\varepsilon$  form. It was known that larger molecules, such as  $n$ -octane, can be clathrated in the  $\varepsilon$  form [30]. All the gas molecules under consideration can easily access the  $\varepsilon$  form. On the other hand, in the S-I form, the slope of  $P(R)$  is larger at around  $R = 1.655 \text{ \AA}$ . Since the size of oxygen and methane is smaller and larger, respectively, than that of

nitrogen, the gas molecules would be effectively filtered in the S-I form.

### 3.3. Solubility of gases

The solubility was calculated by the particle insertion method. Figure 5 shows distribution of  $f(u) \exp(-u/RT)$ , where  $f(u)$  is the distribution function of  $u$  of insertion trials. The value of  $\mu_r$  is related to the area of the distribution as

$$\mu_r = -k_B T \ln \left[ \int_{-\infty}^{\infty} f(u) \exp(-u/k_B T) du \right]. \quad (4)$$

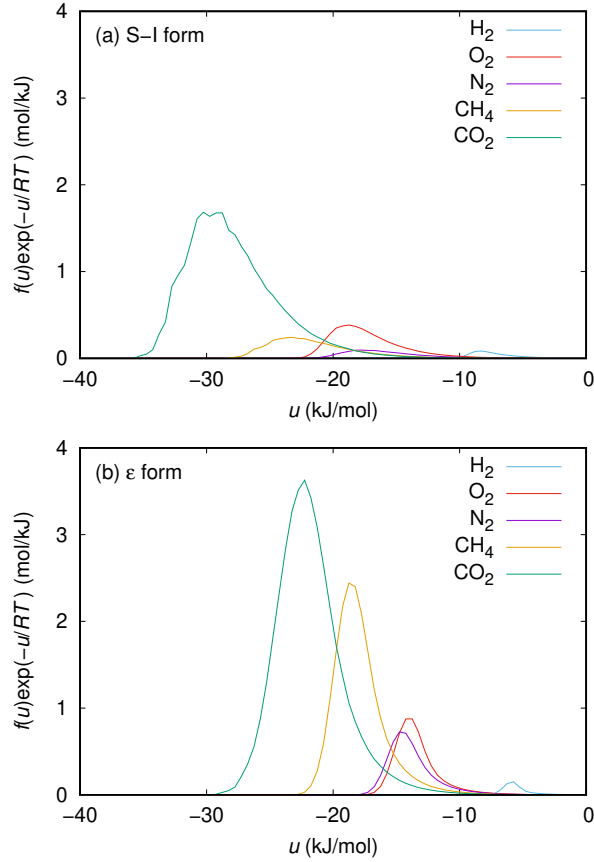


Figure 5: Plot of  $f(u) \exp(-u/k_B T)$  vs.  $u$ , where  $u$  is energy difference before and after each insertion trial.

In the  $\varepsilon$  form, the distribution reflects mainly the attractive interaction between gas and polymer, rather than the repulsive interaction between atom cores, because the channel size is wide compared to the gas molecules,

as seen in Fig. 3. The attractive interaction can be roughly estimated from the sum of LJ energy parameters,  $\varepsilon_{\text{LJ}}$  in Table 1, and in the order of

$$\text{CO}_2 > \text{CH}_4 > \text{O}_2 > \text{N}_2 > \text{H}_2. \quad (5)$$

Therefore, the distribution for  $\text{CO}_2$  spreads over lower  $u$  regions. This leads to the slightly ragged curve for  $\text{CO}_2$  in Fig. 5 because the curve is obtained by products of small  $f(u)$  and large  $\exp(-u/k_{\text{B}}T)$  at lower energy regions. However, the standard error of  $\mu_{\text{r}}$  is sufficiently small (Table 4). The sampling is precise enough to evaluate  $\mu_{\text{r}}$  and  $S$  for all the gases.

In the S-I form, the repulsive interaction, as well as the attractive one is important, because the cavity size is rather small. As seen from Fig. 3, the  $\text{CO}_2$  molecule suitably matches with the size and shape of the ellipsoidal cavity in the S-I form. The three atoms of  $\text{CO}_2$  reside within the attractive interaction region with cavity wall. Therefore, the distribution of  $\text{CO}_2$  in the S-I form spread over further lower  $u$  regions than that in the  $\varepsilon$  form. On the other hand, the  $\text{N}_2$  molecule is slightly fatter compared to the minor axis of the ellipsoidal cavity, as can be estimated from the LJ size parameter  $\sigma_{\text{LJ}}$  in Table 1. The repulsive interaction between  $\text{N}_2$  molecule and cavity wall suppresses the accessible volumes for  $\text{N}_2$ . This leads to the lower height of the distribution for  $\text{N}_2$ .

Table 4: Excess chemical potential  $\mu_{\text{r}}$  and solubility  $S$  of gases in the S-I and  $\varepsilon$  forms.<sup>a</sup>

gas	$\mu_{\text{r}}$ (kJ/mol)		$S$ (cm <sup>3</sup> (STP)/cm <sup>3</sup> atm)	
	S-I form	$\varepsilon$ form	S-I form	$\varepsilon$ form
H <sub>2</sub>	3.0365 (0.0008)	3.1226 (0.0002)	0.26953 (0.00001)	0.26038 (0.000002)
O <sub>2</sub>	-2.001 (0.005)	-2.641 (0.0009)	2.031 (0.004)	2.625 (0.0010)
N <sub>2</sub>	1.176 (0.012)	-2.341 (0.0012)	0.5682 (0.0007)	2.327 (0.0011)
CH <sub>4</sub>	-1.411 (0.024)	-5.658 (0.0021)	1.603 (0.011)	8.80 (0.028)
CO <sub>2</sub>	-6.437 (0.041)	-7.495 (0.0018)	12.0 (1.0)	18.4 (0.11)

<sup>a</sup>Standard errors in parenthesis.

The  $\mu_{\text{r}}$  values, which were calculated by eq. 2, and  $S$  values are tabulated in Table 4. In the S-I form the solubility of  $\text{CO}_2$  is markedly higher than that of  $\text{N}_2$  or  $\text{CH}_4$ .

### 3.4. Gas diffusion in S-I form

Long time simulation runs were performed to investigate diffusion behavior of gases in the S-I and  $\varepsilon$  forms. The animations of  $\text{CO}_2$  and  $\text{N}_2$  diffusion in the S-I form viewed in the  $a$ - $b$  or  $a$ - $c$  plane are supplied as Movie

S1–S4. Snapshots at the moment of jump event of gases are also shown in Fig. 6, which were extracted from the movie files.

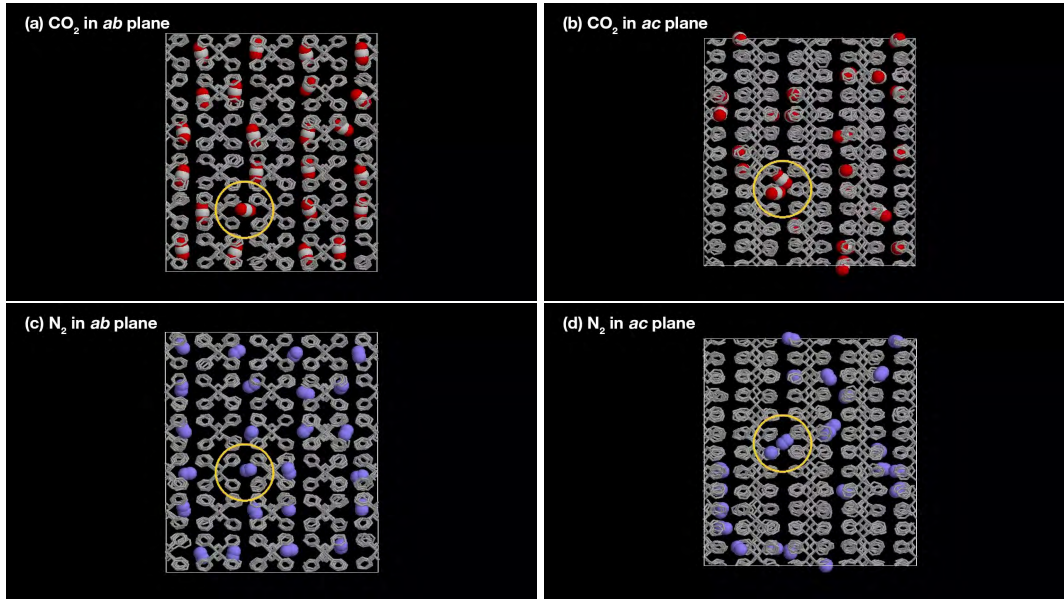


Figure 6: Snapshots at the moment of jump event of gases in s-PS S-I form. The pictures were extracted from movie files movie-S1-CO2-ab.mp4, movie-S2-CO2-ac.mp4, movie-S3-N2-ab.mp4, and movie-S4-N2-ac.mp4 for panel (a), (b), (c), and (d), respectively. The jump events occur at the position indicated by yellow circles.

The gas molecules perform jump diffusion in the zigzag channels along the  $c$ -axis (Movie S2 and S4). A snapshot at the moment of the jump event of  $\text{CO}_2$  is also shown in Fig. S2, where the jump path between the cavities is drawn by the arrows. The jump probability of  $\text{CO}_2$  is rather higher compared with that of  $\text{N}_2$ . In the  $a$ - $b$  plane, the  $\text{CO}_2$  molecules are mainly oriented along the  $b$ -axis and oscillate around that orientation (Movie S1). A perpendicular orientation is sometimes observed, where the  $\text{CO}_2$  molecule is just jumping to the neighbor cavity through the narrow channel (Fig. S2). As for  $\text{N}_2$ , the molecules are frequently rotating in each cavity (Movie S3). This difference in molecular motion leads to an effective transport mechanism of tri-atomic molecules in the S-I form, as discussed in a later subsection.

The displacement of  $\text{CO}_2$  in the s-PS crystal is shown in Fig. 7. The diffusion occurs only along the  $c$ -axis. Its behavior is effectively one-dimensional. As for the S-I form, the diffusion process consists of oscillation in the cavity and jump motion between neighboring cavities. On the contrary, the jump motion is not so clear in the  $\epsilon$  form; the gas transport is rather continuous, reflecting the wide channels. The mean-square displacements

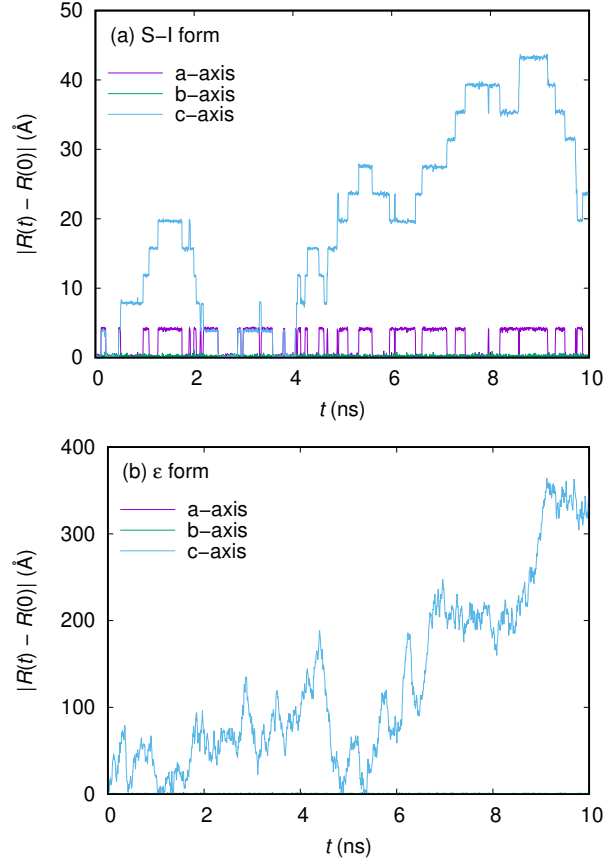


Figure 7: Displacement of one of CO<sub>2</sub> molecules along each axis in s-PS S-I (a) and ε (b) form crystal.

(MSD) of the gas molecules are shown in Fig. 8. The H<sub>2</sub> molecule diffuses most quickly because it is the smallest molecule, while methane diffuses most slowly.

Diffusion coefficients were calculated from the slopes of the MSD. Obtained diffusion coefficients are listed in Table 5. Diffusion coefficients in the ε form are approximately 2 orders larger than those in the S-I form. This is due to the wide tube-like channels in the ε form. In the ε form, however, the difference in diffusivity between the gas species is very small, as indicated by the relative diffusion coefficients. All the gas molecules can diffuse rapidly in the ε form. On the other hand, in the S-I form, the  $D$  values are greatly different for different gas species. The diffusion coefficient of CO<sub>2</sub> is ten times higher than that of N<sub>2</sub>. It is difficult to achieve such a sharp difference in diffusivity using amorphous membranes, because of their broad distribution of free volumes.

The remarkable point is that the tri-atomic molecule, CO<sub>2</sub>, diffuses more quickly than the di-atomic molecules

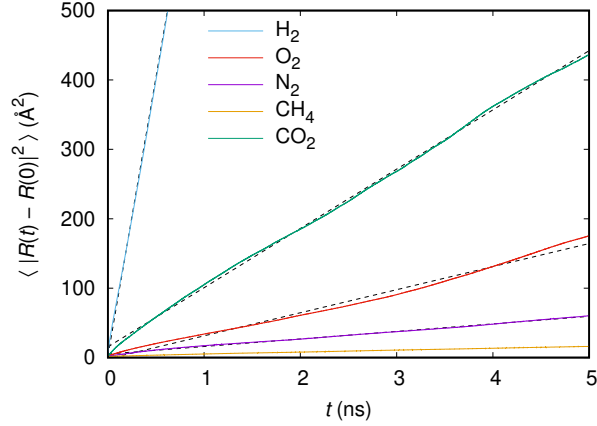


Figure 8: Mean-square displacement (MSD) of gases in s-PS S-I form crystal. The MSD values are fitted to linear lines (dashed lines) by the least-squares method.

Table 5: Diffusion coefficient of gases along  $c$ -axis,  $D_c$ , in the S-I and  $\varepsilon$  forms. Relative diffusion coefficient,  $D_c/D_c^{\text{CO}_2}$ , is also tabulated.

gas	$D_c \times 10^5 \text{ (cm}^2/\text{s)}^a$		$D_c/D_c^{\text{CO}_2}$	
	S-I form	$\varepsilon$ form	S-I form	$\varepsilon$ form
H <sub>2</sub>	4.03 (0.82)	270 (74)	7.9	6.9
O <sub>2</sub>	0.144 (0.045)	39 (13)	0.28	1.0
N <sub>2</sub>	0.060 (0.015)	48 (6)	0.12	1.2
CH <sub>4</sub>	0.008 (0.003)	69 (13)	0.02	1.8
CO <sub>2</sub>	0.51 (0.22)	39 (11)	1	1

<sup>a</sup>Standard errors in parenthesis.

O<sub>2</sub> and N<sub>2</sub>, in the S-I form. In other words, larger molecules can diffuse more quickly in the S-I form. This anomaly is not observed for the  $\varepsilon$  form.

### 3.5. Prediction of permeability and selectivity

The permeability was calculated by

$$P = DS, \quad (6)$$

on the basis of solution–diffusion model [70]. Table 6 lists the predicted permeability  $P$  and CO<sub>2</sub> selectivity. Obviously, the solubility of CO<sub>2</sub> in the S-I form is higher than that of other gases. Combined with effective diffusion of CO<sub>2</sub>, the permeability of CO<sub>2</sub> in the S-I form becomes very high; approximately two hundred times higher than that of N<sub>2</sub>. This leads to higher CO<sub>2</sub> selectivity in the S-I form. The CO<sub>2</sub> selectivity is very high in the S-I form, especially for the target gases N<sub>2</sub> and CH<sub>4</sub>. It is expected that the S-I membrane could be used for high efficiency carbon-capture systems installed in power plants (CO<sub>2</sub>/N<sub>2</sub>) or natural gas fields (CO<sub>2</sub>/CH<sub>4</sub>).

Table 6: Predicted permeability  $P$  and CO<sub>2</sub> selectivity in the S-I and  $\epsilon$  forms.

gas	$P$ (Barrer) <sup>a</sup>		CO <sub>2</sub> selectivity <sup>b</sup>	
	S-I form	$\epsilon$ form	S-I form	$\epsilon$ form
H <sub>2</sub>	$1.4 \times 10^3$	$9.2 \times 10^4$	5.6	10.2
O <sub>2</sub>	$3.8 \times 10^2$	$1.4 \times 10^5$	21	7.0
N <sub>2</sub>	$4.5 \times 10^1$	$1.5 \times 10^5$	177	6.4
CH <sub>4</sub>	$1.7 \times 10^1$	$7.9 \times 10^5$	460	1.2
CO <sub>2</sub>	$8.0 \times 10^3$	$9.5 \times 10^5$		

<sup>a</sup>Barrer =  $10^{-10}$  cm<sup>3</sup>(STP)cm/s cm<sup>2</sup>cmHg.

<sup>b</sup>Calculated by  $P_{\text{CO}_2}/P_{\text{gas}}$ .

### 3.6. Comparison to experiments

The permeabilities of gases in amorphous and semicrystalline  $\alpha$  form of s-PS were reported by Hodge et al. [37], as tabulated in Table 7. Because amorphous s-PS is glassy state at room temperature, which is lower than glass transition temperature  $T_g \sim 370$  K, the diffusion coefficients are small in amorphous s-PS. The  $D$  values were reported to be enhanced 2–3 times in the semicrystalline sample with crystallinity 0.3 [37]. This enhancement was attributed to gas permeable channels in the crystals dispersed in amorphous regions. The enhancement of permeability in semicrystalline samples compared to amorphous ones is also reported for poly(2,6-dimethyl-1,4-phenylene)oxide (PPO) [71], which has also nanoporous-crystalline phase [72, 73]. These behaviors are contrasted with gas diffusion process in ordinary semicrystalline polymers such as polyethylene, in which diffusion paths are limited to rubbery amorphous region [74].

The calculated diffusion coefficients of CO<sub>2</sub> in s-PS S-I and  $\epsilon$  forms are  $5.1 \times 10^{-6}$  and  $3.9 \times 10^{-4}$ , respectively, which are significantly large compared to that in amorphous s-PS,  $4.0 \times 10^{-8}$ . This is owing to the porous nature

of these crystals, as evidenced by Fig. 3 and 4.

Table 7: Experimental values of  $S$ ,  $D$ , and  $P$  of gases in s-PS at 298 K [37].

gas	$S$ (cm <sup>3</sup> (STP)/cm <sup>3</sup> atm)	$D$ (cm <sup>2</sup> /s)	$P$ (Barrer)
amorphous			
O <sub>2</sub>	0.17	$1.1 \times 10^{-7}$	2.5
CO <sub>2</sub>	2.9	$4.0 \times 10^{-8}$	15
$\alpha$ form crystal <sup>a</sup>			
O <sub>2</sub>	0.10	$3.6 \times 10^{-7}$	4.6
CO <sub>2</sub>	1.8	$8.2 \times 10^{-8}$	17

<sup>a</sup>Crystallinity determined by X-ray diffraction is approximately 0.3.

The separation performance of the S-I form is compared to known commercial membranes in Fig. 9. Because of competing nature of permeability and selectivity, the commercial membranes are distributed below the upper-bound line which has a negative slope. The performance of the S-I form is far beyond the upper-bound as shown by the star in the figure.

### 3.7. Origin of effective and efficient transport

The solubility is mainly dependent on the interaction between the gas molecule and the host matrix. Especially in the molecular cavities in the crystal, the repulsive interaction is severely affected by matching in the size and shape between guests and cavities. Consulting Figs. 1 and 3, the matching is good for CO<sub>2</sub>, which is just fitted to the ellipsoidal cavity in the S-I form. Because of the strong attractive interaction and the comfortable matching to the cavity shape and size, the solubility of CO<sub>2</sub> becomes high in the S-I form.

The diffusion process of small penetrants in dense amorphous polymers have been understood as “jump diffusion”, i.e., a series of hopping events between voids [74]. This kind of motion has been clearly observed by MD simulations. The transition state theory has also been applied [74–76], in which the rates of solute’s hops are dependent on the energy barrier (at the transition state) between voids.

In the s-PS S-I crystal, the diffusion scheme of gases is also jump diffusion, as evidenced from the movies (Movie S1–S4) and the displacements of gases (Fig. 7). In contrast, the jump motion is not so clear in the  $\epsilon$  form, where the gas transport is rather continuous. The difference can be attributed to existence of energy barrier. A hopping process in the S-I form is shown schematically in Fig. 10. The CO<sub>2</sub> molecule is oscillating

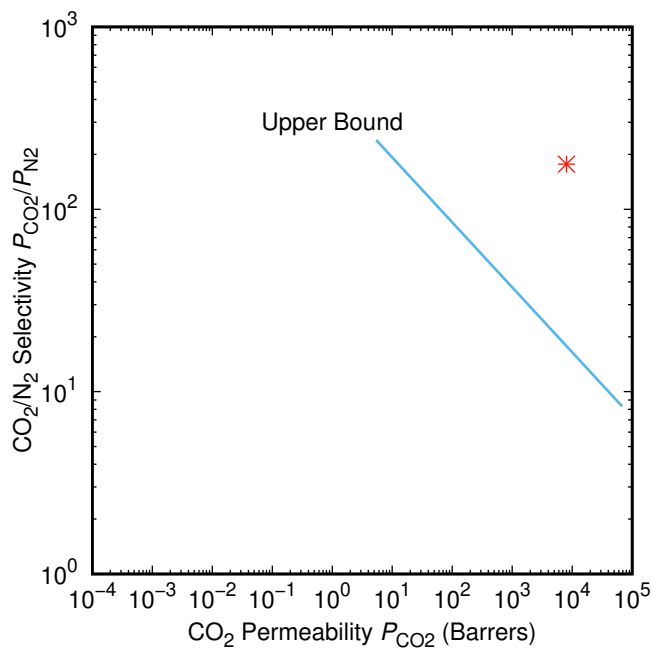


Figure 9: Upper bound correlation for  $\text{CO}_2/\text{N}_2$  separation, summarized by Robeson [1]. The  $\text{CO}_2$  selectivity is plotted against permeability of  $\text{CO}_2$  for various commercial membranes. The star in the upper right indicates the predicted values for the s-PS S-I form (this work).

most of the time in the individual cavity, interacting with host matrix (left and right panels), and the jump motion sometimes occurs through the narrow channel between neighbor cavities (middle panel).

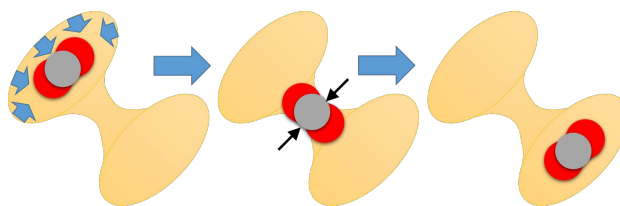


Figure 10: Jump-diffusion scheme of  $\text{CO}_2$  in s-PS S-I form.

In the S-I form, the diffusion process can be treated as a one-dimensional random walk. The jump length can approximately be treated as constant, defined by crystalline periodicity. Therefore, the diffusion coefficient is dependent solely on the jump probability. The jump probability is mainly governed by the transition state (middle panel of Fig. 10) of individual jump event, and expected to be proportional to the Boltzmann factor

of the activation energy. The activation energy of the jump event is thought to be affected by the short-axis length of the gas molecule. Although the long-axis length of  $\text{CO}_2$  is the largest, the short-axis length is smaller than that of  $\text{N}_2$  or  $\text{CH}_4$ , and almost the same as that of  $\text{O}_2$ . Therefore, the diffusion coefficient of  $\text{CO}_2$  becomes larger than that of  $\text{N}_2$  or  $\text{CH}_4$ .

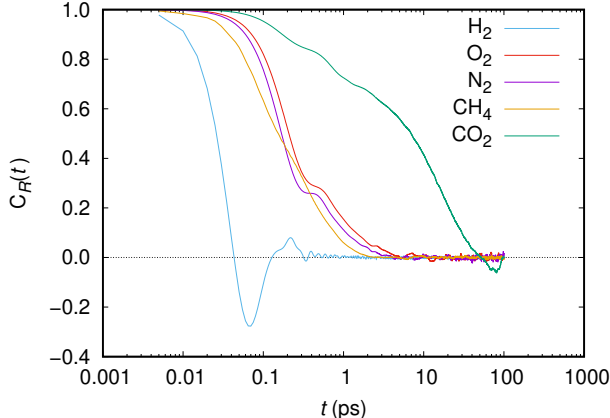


Figure 11: Re-orientational auto-correlation function of gases in s-PS S-I form crystal.

However, the latter raises an important question. Why is it that the diffusion coefficient of  $\text{CO}_2$  is four times larger than that of  $\text{O}_2$ , in spite of their similar diameters? Please recall the animation of diffusion behavior of  $\text{CO}_2$  and  $\text{N}_2$  in Supporting Information.  $\text{CO}_2$  molecules are oscillating in the cavity, while  $\text{N}_2$  molecules are rotating. This is because the full length (long-axis length) of the  $\text{CO}_2$  molecule is too long to re-orient in the ellipsoidal cavity. From the re-orientational auto-correlation function of gases, Fig. 11, the re-orientational relaxation time of  $\text{CO}_2$  is confirmed to be two orders longer than those of  $\text{O}_2$  and  $\text{N}_2$ .

From these observations, the author proposes that the momentum transfer from polymer matrices is effectively delivered to the translational degree of freedom for a tri-atomic molecule. For di-atomic molecules, the impulses from polymer chains are transferred into angular momentum. The gas molecules spin in the cavity. Therefore, the impulses from the matrices do not lead to jump trials. In contrast, for tri-atomic molecules, the transferred momentum is effectively used for translation, because  $\text{CO}_2$  molecules cannot rotate in the cavity. In other words,  $\text{CO}_2$  molecules more frequently exchange their momentum to the host matrix. This leads to an increase in jump trials.

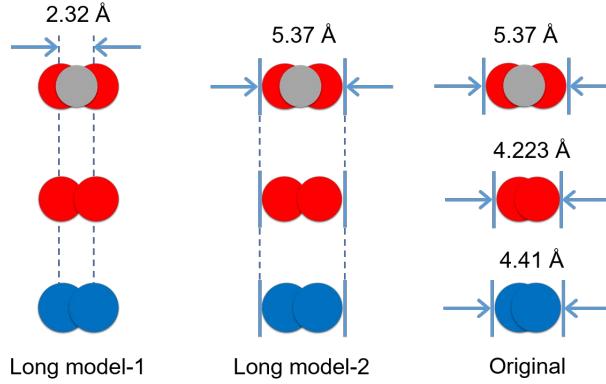


Figure 12: “Long-gas” model of O<sub>2</sub> (middle) and N<sub>2</sub> (bottom), compared with CO<sub>2</sub> (top).

Table 8: Force-field parameters for “long-gas” model

gas	atom	model-1 <sup>a</sup>		model-2 <sup>b</sup>	
		$q$ (e)	$l_b$ (Å)	$q$ (e)	$l_b$ (Å)
N <sub>2</sub>	N	-0.1084	1.16	-0.1374	1.03
	M	+0.2168		+0.2748	
O <sub>2</sub>	O	-0.0350	1.16	-0.0324	1.1785
	M	+0.0670		+0.0648	

<sup>a</sup>Same bond length as CO<sub>2</sub>.

<sup>b</sup>Same full-length as CO<sub>2</sub>.

### 3.8. Proof by “long-gas” model

In order to substantiate this hypothesis, an MD simulation was performed using the “long-gas” models shown in Fig. 12. In model-1, O–O and N–N bond lengths (originally 1.21 and 1.10 Å, respectively) are elongated to the same length as C–C of CO<sub>2</sub> ( $2l_b = 2.32$  Å). In model-2, bond lengths of di-atomic molecules are adjusted so that their molecular full lengths are identical to that of CO<sub>2</sub> ( $2l_b + \sigma_{\text{OO}} = 5.37$  Å). The partial charges of atoms were adjusted to reproduce quadrupole moments of original models. The model parameters are listed in Table 8.

The calculated diffusion coefficients for the long-gas model are listed in Table 9. Using the model, the diffusion coefficients were surely enhanced, approximately 5–10 times. The  $D$  values of O<sub>2</sub> and N<sub>2</sub> calculated

for the long model were approximately the same as that of CO<sub>2</sub>,  $0.51 \times 10^{-5}$  cm<sup>2</sup>/s. It is revealed that matching of molecular structure with cavity shape is important for control of diffusivity in the crystalline membrane.

Table 9: Diffusion coefficients calculated for “long-gas” models.

gas	$D_c \times 10^5$ (cm <sup>2</sup> /s)		
	model-1	model-2	original
S-I form			
O <sub>2</sub>	0.61 (0.07)	0.70 (0.07)	0.144
N <sub>2</sub>	0.61 (0.15)	0.32 (0.05)	0.060
$\varepsilon$ form			
O <sub>2</sub>	43 (2)	43 (5)	39
N <sub>2</sub>	55 (13)	43 (4)	48

### 3.9. Design criteria for crystalline membrane

These findings suggest a novel design criteria for CO<sub>2</sub> separation membranes using porous polymer crystals. For crystalline membranes, it is important to control mesh size and affinity, which affect both diffusivity and solubility. In addition, diffusivity can be controlled by matching in shape between cavity and gas molecule. Indeed, in some cases, larger molecules can diffuse more quickly; diffusion coefficient of CO<sub>2</sub> is larger than that of O<sub>2</sub> and N<sub>2</sub>. As evidenced from the present simulation, the momentum of the polymer matrix is effectively transferred to the translational degree of freedom of CO<sub>2</sub> molecules. A novel aspects, controlling the momentum transfer between matrices and penetrants by coupling to the re-orientational motion of gases in regular cavities, could be introduced into the design criteria.

For amorphous membranes, as contrasted with the crystalline membranes, separation by diffusivity is insufficient because of the broad distribution of the activation energy at the transition state. Furthermore, it is difficult to control the momentum transfer of gas molecules in amorphous polymers because of a wide variety of cavity size and shape.

From a technological point of view, we have to overcome the difficulty that the crystallinity is generally low (up to 50 % or so) and complex spherulites are formed for polymer systems. The best performance of separation, presented in this article, can be achieved for oriented single crystals. The solvent crystallization on

the solid surface may be promising to obtain oriented single crystals; the crystal size and orientation of the s-PS  $\delta$  form can be controlled by solvent species, using host–guest interactions between polymer and solvents [77]. If once the oriented single crystal of the  $\delta$  form is obtained, it may be transformed into the  $\varepsilon$  form by a solvent treatment and further transformed into the S-I form by applying stress. A confined crystallization in polymer nanolayered films may also be used to obtain oriented nano-crystals [78].

Note that the design criteria proposed above is not specific to the s-PS S-I form, but may be widely applicable to the design of separation membranes with ordered structures. One of the limitation of the S-I form to use for gas separation is that it needs stress to keep its structure. It is challenging to search for other crystals with similar cavity structures even under atmospheric pressure, by applying the design criteria. Following the design criteria, the permeability of other tri-atomic molecules, for example,  $\text{N}_2\text{O}$  (full length  $\sim 5.4$  Å, known as greenhouse gas), may be enhanced;  $\text{N}_2\text{O}$  may be effectively captured from the air.

#### 4. Conclusions

The crystal structure of a new orthorhombic “S-I” form of s-PS under uniaxial stress ( $\sigma_{yy} = 0.27$  GPa) was determined by MD simulations. The space group is  $Pbcb$  and the lattice constants are  $a = 10.96$  Å,  $b = 16.55$  Å, and  $c = 7.87$  Å. The density is  $0.969$  g/cm<sup>3</sup>, which is almost the same as that of the empty  $\delta_e$  form. In the S-I form, chains with relaxed L and L (or R and R) contacts form zigzag channels at the molecular level.

It was predicted that the S-I membrane could have significantly higher  $\text{CO}_2/\text{N}_2$  ( $\sim 180$ ) and  $\text{CO}_2/\text{CH}_4$  ( $\sim 500$ ) separation factors with preserving its high  $\text{CO}_2$  permeability 8000 Barrers. The mechanism of the effective  $\text{CO}_2$  transport in the S-I form was elucidated in detail. The  $\text{CO}_2$  molecule is just fitted to the ellipsoidal cavities in the S-I form and effectively interacts with surrounding polymer matrix. This leads to the higher solubility of  $\text{CO}_2$ .

In addition to this, tri-atomic molecules can more effectively diffuse in the S-I form, compared with di-atomic molecules. The  $\text{CO}_2$  molecule is oscillating, while the  $\text{N}_2$  and  $\text{O}_2$  molecules are rotating in the ellipsoidal cavities. The momentum from the polymer matrix is effectively transformed into translational motion for  $\text{CO}_2$ , while it is transferred into rotational degree of freedom for  $\text{N}_2$  and  $\text{O}_2$ . As a result, the diffusion coefficient of  $\text{CO}_2$  becomes higher than that of  $\text{N}_2$  and  $\text{O}_2$ . The effect of long-axis length of gas molecules on diffusivity was confirmed by the “long-gas” model, in which the lengths of  $\text{N}_2$  and  $\text{O}_2$  were elongated to the same length as that of  $\text{CO}_2$ . The diffusion coefficients of di-atomic molecules were surely enhanced by the long-gas model.

Because of the enhanced solubility and diffusivity, the permeability of  $\text{CO}_2$  becomes extremely higher in

the S-I form; CO<sub>2</sub> can be effectively separated from the mixed gas with N<sub>2</sub> or CH<sub>4</sub>. To design high-efficiency CO<sub>2</sub> transport membranes, it is important to control the momentum transfer from polymer matrix to the translational degree of freedom of the penetrant.

## Acknowledgments

This work was partly supported by JSPS KAKENHI, grant number 19550121. The calculations were performed on supercomputer at ACCMS, Kyoto University. The fee of the supercomputer was supported by CII, University of Fukui.

## Appendix A. Calculation of X-ray intensity

The structure factor  $F_{hkl}$  for the Miller index  $(hkl)$  was calculated by

$$F_{hkl} = \sum_j f_j T_j \exp [2\pi i(hx_j + ky_j + lz_j)], \quad (\text{A.1})$$

where  $f_j$  is the atomic scattering factor of atom  $j$ ,  $T_j$  is the temperature factor ( $B = 8 \text{ \AA}^2$ ),  $i$  is the imaginary unit, and  $(x_j, y_j, z_j)$  is the fractional coordinate of atom  $j$ . Hydrogen atoms were also included in the calculation. The reciprocal lattice vector  $\mathbf{k} = h\mathbf{a}^* + k\mathbf{b}^* + l\mathbf{c}^*$ , where  $\mathbf{a}^*$ ,  $\mathbf{b}^*$ , and  $\mathbf{c}^*$  are the reciprocal primitive vectors, is related to the diffraction angle  $2\theta$  by:

$$|\mathbf{k}| = \frac{2 \sin \theta}{\lambda}, \quad (\text{A.2})$$

where  $\lambda = 1.5418 \text{ \AA}$  is the wavelength of the Cu K $\alpha$  radiation. The  $f_j$  value is approximated by:

$$f = \sum_{p=1}^4 a_p \exp \left( -\frac{b_p \sin^2 \theta}{\lambda^2} \right) + c, \quad (\text{A.3})$$

where the parameters  $a_p$ ,  $b_p$ , and  $c$  are published for each element [79]. The  $F_{hkl}$  values were calculated for sets of  $h$ ,  $k$ , and  $l$  satisfying  $\sqrt{h^2 + k^2 + l^2} \leq 7$ . The X-ray diffraction intensity  $I_{hkl}$  was calculated by:

$$I_{hkl} = |F_{hkl}|^2 Lp, \quad (\text{A.4})$$

where  $Lp$  is the Lorentz polarization factor for X-ray powder diffraction:

$$Lp = \frac{1 + \cos^2 2\theta}{2 \sin^2 \theta \cos \theta}. \quad (\text{A.5})$$

## Appendix B. Supplementary data

Supplementary material related to this article can be found online at <https://doi.org/10.1016/j.memsci.2021.120202>.

## References

- [1] L. M. Robeson, The upper bound revisited, *J. Membr. Sci.* 320 (1) (2008) 390–400. doi:10.1016/j.memsci.2008.04.030.
- [2] H. B. Park, J. Kamcev, L. M. Robeson, M. Elimelech, B. D. Freeman, Maximizing the right stuff: The trade-off between membrane permeability and selectivity, *Science* 356 (6343) (2017) eaab0530. doi:10.1126/science.aab0530.
- [3] Y. Tamai, M. Fukuda, Nanoscale molecular cavity in crystalline polymer membranes studied by molecular dynamics simulation, *Polymer* 44 (11) (2003) 3279–3289. doi:10.1016/s0032-3861(03)00214-3.
- [4] Z. Liu, J. Yuan, J. M. van Baten, J. Zhou, X. Tang, C. Zhao, W. Chen, X. Yi, R. Krishna, G. Sastre, A. Zheng, Synergistically enhance confined diffusion by continuum intersecting channels in zeolites, *Sci. Adv.* 7 (2021) eabf0775. doi:10.1126/sciadv.abf0775.
- [5] A. Hasanzadeh, S. Pakdel, J. Azamat, H. Erfan-Niya, A. Khataee, The removal of nitrogen monoxide from polluted air using cha- and ddr-type zeolite membranes: Insights from molecular simulations, *Mater. Today Commun.* 28 (2021) 102651. doi:10.1016/j.mtcomm.2021.102651.
- [6] Z. Yuan, A. G. Rajan, R. P. Misra, L. W. Drahushuk, K. V. Agrawal, M. S. Strano, D. Blankschtein, Mechanism and prediction of gas permeation through sub-nanometer graphene pores: Comparison of theory and simulation, *ACS Nano* 11 (2017) 7974–7987. doi:10.1021/acsnano.7b02523.
- [7] Z. Yuan, R. P. Misra, A. G. Rajan, M. S. Strano, D. Blankschtein, Analytical prediction of gas permeation through graphene nanopores of varying sizes: Understanding transitions across multiple transport regimes, *ACS Nano* 13 (2019) 11809–11824. doi:10.1021/acsnano.9b05779.
- [8] G. Bayat, R. Saghatchi, J. Azamat, A. Khataee, Separation of methane from different gas mixtures using modified silicon carbide nanosheet: Micro and macro scale numerical studies, *Chin. J. Chem. Eng.* 28 (2020) 1268–1276. doi:10.1016/j.cjche.2019.12.005.

- [9] J. Azamat, A. Khataee, MoS<sub>2</sub> nanosheet as a promising nanostructure membrane for gas separation, *J. Ind. Eng. Chem.* 66 (2018) 269–278. doi:10.1016/j.jiec.2018.05.040.
- [10] G. Milano, G. Guerra, Understanding at molecular level of nanoporous and co-crystalline materials based on syndiotactic polystyrene, *Prog. Mater. Sci.* 54 (1) (2009) 68–88. doi:10.1016/j.pmatsci.2008.07.001.
- [11] G. Guerra, C. Daniel, P. Rizzo, O. Tarallo, Advanced materials based on polymer cocrystalline forms, *J. Polym. Sci. Part B: Polym. Phys.* 50 (5) (2012) 305–322. doi:10.1002/polb.23035.
- [12] E. B. Gowd, K. Tashiro, C. Ramesh, Structural phase transitions of syndiotactic polystyrene, *Prog. Polym. Sci.* 34 (3) (2009) 280–315. doi:10.1016/j.progpolymsci.2008.11.002.
- [13] O. Greis, Y. Xu, T. Asano, J. Petermann, Morphology and structure of syndiotactic polystyrene, *Polymer* 30 (4) (1989) 590–594. doi:10.1016/0032-3861(89)90140-7.
- [14] C. De Rosa, G. Guerra, V. Petraccone, P. Corradini, Crystal structure of the  $\alpha$ -form of syndiotactic polystyrene, *Polym. J.* 23 (12) (1991) 1435–1442. doi:10.1295/polymj.23.1435.
- [15] C. De Rosa, Crystal structure of the trigonal modification ( $\alpha$  form) of syndiotactic polystyrene, *Macromolecules* 29 (26) (1996) 8460–8465. doi:10.1021/ma960905q.
- [16] L. Cartier, T. Okihara, B. Lotz, The  $\alpha''$  “superstructure” of syndiotactic polystyrene: A frustrated structure, *Macromolecules* 31 (10) (1998) 3303–3310. doi:10.1021/ma9719059.
- [17] C. De Rosa, M. Rapacciuolo, G. Guerra, V. Petraccone, P. Corradini, On the crystal structure of the orthorhombic form of syndiotactic polystyrene, *Polymer* 33 (7) (1992) 1423–1428. doi:10.1016/0032-3861(92)90117-f.
- [18] Y. Chatani, Y. Shimane, T. Ijitsu, T. Yukinari, Structural study on syndiotactic polystyrene: 3. crystal structure of planar form I, *Polymer* 34 (8) (1993) 1625–1629. doi:10.1016/0032-3861(93)90319-6.
- [19] Y. K. Wang, J. D. Savage, D. Yang, S. L. Hsu, Morphological study of phase transition behavior in syndiotactic polystyrene, *Macromolecules* 25 (14) (1992) 3659–3666. doi:10.1021/ma00040a009.
- [20] P. Rizzo, M. Lamberti, A. R. Albuñia, O. Ruiz de Ballesteros, G. Guerra, Crystalline orientation in syndiotactic polystyrene cast films, *Macromolecules* 35 (15) (2002) 5854–5860. doi:10.1021/ma011853u.

- [21] Y. Tamai, M. Fukuda, Thermally induced phase transition of crystalline syndiotactic polystyrene studied by molecular dynamics simulation, *Macromol. Rapid Commun.* 23 (15) (2002) 891–895. doi:10.1002/1521-3927(20021001)23:15<891::aid-marc891>3.0.co;2-8.
- [22] Y. Tamai, Guest occupation effects on the transition of crystalline syndiotactic polystyrene: Selection criteria for fundamental structures  $\gamma$ -I and  $\gamma$ -II, *Macromol. Theory Simul.* (2018) 1800039doi:10.1002/mats.201800039.
- [23] Y. Chatani, Y. Shimane, T. Inagaki, T. Ijitsu, T. Yukinari, H. Shikuma, Structural study on syndiotactic polystyrene: 2. crystal structure of molecular compound with toluene, *Polymer* 34 (8) (1993) 1620–1624. doi:10.1016/0032-3861(93)90318-5.
- [24] Y. Chatani, T. Inagaki, Y. Shimane, H. Shikuma, Structural study on syndiotactic polystyrene: 4. formation and crystal structure of molecular compound with iodine, *Polymer* 34 (23) (1993) 4841–4845. doi:10.1016/0032-3861(93)90007-w.
- [25] C. De Rosa, P. Rizzo, O. de Ballesteros, V. Petraccone, G. Guerra, Crystal structure of the clathrate  $\delta$  form of syndiotactic polystyrene containing 1,2-dichloroethane, *Polymer* 40 (8) (1999) 2103–2110. doi:10.1016/s0032-3861(97)10372-x.
- [26] C. De Rosa, G. Guerra, V. Petraccone, B. Pirozzi, Crystal structure of the emptied clathrate form ( $\delta_e$  form) of syndiotactic polystyrene, *Macromolecules* 30 (14) (1997) 4147–4152. doi:10.1021/ma970061q.
- [27] P. Rizzo, C. Daniel, A. De Girolamo Del Mauro, G. Guerra, New host polymeric framework and related polar guest cocrystals, *Chem. Mater.* 19 (16) (2007) 3864–3866. doi:10.1021/cm071099c.
- [28] V. Petraccone, O. Ruiz de Ballesteros, O. Tarallo, P. Rizzo, G. Guerra, Nanoporous polymer crystals with cavities and channels, *Chem. Mater.* 20 (11) (2008) 3663–3668. doi:10.1021/cm800462h.
- [29] O. Tarallo, V. Petraccone, A. R. Albuñia, C. Daniel, G. Guerra, Monoclinic and triclinic  $\delta$ -clathrates of syndiotactic polystyrene, *Macromolecules* 43 (20) (2010) 8549–8558. doi:10.1021/ma1013513.
- [30] O. Tarallo, M. M. Schiavone, Syndiotactic polystyrene  $\epsilon$  cocrystals with  $n$ -alkanes: Guest uptake and crystal structure, *Soft Mater.* 9 (2-3) (2011) 124–140. doi:10.1080/1539445x.2011.552349.
- [31] M. R. Acocella, P. Rizzo, C. Daniel, O. Tarallo, G. Guerra, Nanoporous triclinic  $\delta$  modification of syndiotactic polystyrene, *Polymer* 63 (2015) 230–236. doi:10.1016/j.polymer.2015.02.058.

- [32] Y. Tamai, Y. Tsujita, M. Fukuda, Reorientational relaxation of aromatic molecules in the molecular cavity of crystalline syndiotactic polystyrene studied by molecular dynamics simulation, *J. Mol. Struct.* 739 (1) (2005) 33–40. doi:10.1016/j.molstruc.2004.04.036.
- [33] H. Kobayashi, O. Urakawa, F. Kaneko, T. Inoue, Dynamics of polar aromatic molecules confined in a nanocavity of  $\delta$ -phase of syndiotactic polystyrene as studied by dielectric spectroscopy, *Chem. Phys.* 479 (2016) 122–128. doi:10.1016/j.chemphys.2016.07.021.
- [34] H. Kobayashi, S. Akazawa, O. Urakawa, F. Kaneko, T. Inoue, Anisotropic dynamics of benzonitrile confined in  $\delta$  and  $\epsilon$  clathrate phases of syndiotactic polystyrene, *Macromolecules* 51 (21) (2018) 8611–8619. doi:10.1021/acs.macromol.8b00799.
- [35] G. Milano, G. Guerra, F. Müller-Plathe, Anisotropic diffusion of small penetrants in the  $\delta$  crystalline phase of syndiotactic polystyrene: A molecular dynamics simulation study, *Chem. Mater.* 14 (7) (2002) 2977–2982. doi:10.1021/cm011297i.
- [36] V. Venditto, A. De Girolamo Del Mauro, G. Mensitieri, G. Milano, P. Musto, P. Rizzo, G. Guerra, Anisotropic guest diffusion in the  $\delta$  crystalline host phase of syndiotactic polystyrene: Transport kinetics in films with three different uniplanar orientations of the host phase, *Chem. Mater.* 18 (9) (2006) 2205–2210. doi:10.1021/cm051657s.
- [37] K. Hodge, T. Prodpran, N. Shenogina, S. Nazarenko, Diffusion of oxygen and carbon dioxide in thermally crystallized syndiotactic polystyrene, *J. Polym. Sci. Part B: Polym. Phys.* 39 (20) (2001) 2519–2538. doi:10.1002/polb.1223.
- [38] T. Prodpran, S. Shenogin, S. Nazarenko, Gas transport behavior of semicrystalline syndiotactic polystyrene containing  $\alpha$  and  $\beta$  crystalline forms, *Polymer* 43 (8) (2002) 2295–2309. doi:10.1016/s0032-3861(02)00026-5.
- [39] Y. Tamai, M. Fukuda, Fast one-dimensional gas transport in molecular capillary embedded in polymer crystal, *Chem. Phys. Lett.* 371 (1) (2003) 217–222. doi:10.1016/s0009-2614(03)00249-5.
- [40] D. Larobina, L. Sanguigno, V. Venditto, G. Guerra, G. Mensitieri, Gas sorption and transport in syndiotactic polystyrene with nanoporous crystalline phase, *Polymer* 45 (2) (2004) 429–436. doi:10.1016/j.polymer.2003.11.009.

- [41] F. De Candia, R. Russo, V. Vittoria, Strain-induced conformational transitions in syndiotactic polystyrene, *Polym. Commun.* 32 (10) (1991) 306–309.
- [42] T. Ouchi, S. Nagasaka, A. Hotta,  $\beta$  to  $\alpha$  form transition observed in the crystalline structures of syndiotactic polystyrene (sPS), *Macromolecules* 44 (7) (2011) 2112–2119. doi:10.1021/ma200166m.
- [43] F. Endo, A. Hotta, Thermal effects on the strain-induced  $\beta$  to  $\alpha$  form crystalline structural transition of solid-state syndiotactic polystyrene, *Polymer* 135 (2018) 103–110. doi:10.1016/j.polymer.2017.12.013.
- [44] Y. Tamai, Molecular dynamics simulations of structural transitions of crystalline polystyrene in response to external stresses and temperatures, *Polymer* 128 (2017) 177–187. doi:10.1016/j.polymer.2017.09.028.
- [45] C. Liu, K. Kremer, T. Berau, Polymorphism of syndiotactic polystyrene crystals from multiscale simulations, *Adv. Theor. Simul.* 1 (7) (2018) 1800024. doi:10.1002/adts.201800024.
- [46] C. Liu, J. G. Brandenburg, O. Valsson, K. Kremer, T. Berau, Free-energy landscape of polymer-crystal polymorphism, *Soft Matter* 16 (2020) 9683–9692. doi:10.1039/d0sm01342k.
- [47] Y. Tamai, Rearrangement of nanoporous cavity structures in crystalline syndiotactic polystyrene associated with stress-induced phase transition, *ACS Macro Lett.* 2 (9) (2013) 834–838. doi:10.1021/mz400386z.
- [48] Y. Tamai, Crystalline polymer membrane with extremely high selectivity for CO<sub>2</sub> predicted by molecular simulation, *Polym. Prep. Jpn.* 62 (2013) 3427–3428.
- [49] W. D. Cornell, P. Cieplak, C. I. Bayly, I. R. Gould, K. M. Merz, D. M. Ferguson, D. C. Spellmeyer, T. Fox, J. W. Caldwell, P. A. Kollman, A second generation force field for the simulation of proteins, nucleic acids, and organic molecules, *J. Am. Chem. Soc.* 117 (19) (1995) 5179–5197. doi:10.1021/ja00124a002.
- [50] J. J. Potoff, J. I. Siepmann, Vapor–liquid equilibria of mixtures containing alkanes, carbon dioxide, and nitrogen, *AIChE J.* 47 (7) (2001) 1676–1682. doi:10.1002/aic.690470719.
- [51] N. Hansen, F. A. B. Agbor, F. J. Keil, New force fields for nitrous oxide and oxygen and their application to phase equilibria simulations, *Fluid Phase Equilib.* 259 (2) (2007) 180–188. doi:10.1016/j.fluid.2007.07.014.
- [52] Q. Yang, C. Zhong, Molecular simulation of carbon dioxide/methane/hydrogen mixture adsorption in metal-organic frameworks, *J. Phys. Chem. B* 110 (36) (2006) 17776–17783. doi:10.1021/jp062723w.

- [53] G. Kaminski, E. M. Duffy, T. Matsui, W. L. Jorgensen, Free energies of hydration and pure liquid properties of hydrocarbons from the OPLS all-atom model, *J. Phys. Chem.* 98 (49) (1994) 13077–13082. doi:10.1021/j100100a043.
- [54] S. Asahi, Y. Tamai, Diffusion mechanism of CO<sub>2</sub> in a crystalline polymer membrane studied using model gases, *Mol. Simul.* 41 (10–12) (2015) 974–979. doi:10.1080/08927022.2014.930571.
- [55] C. S. Murthy, K. Singer, I. R. McDonald, Interaction site models for carbon dioxide, *Mol. Phys.* 44 (1) (1981) 135–143. doi:10.1080/00268978100102331.
- [56] J. Fischer, S. Lago, Thermodynamic perturbation theory for molecular liquid mixtures, *J. Chem. Phys.* 78 (1983) 5750–5758. doi:10.1063/1.445458.
- [57] P. S. Y. Cheung, J. G. Powles, The properties of liquid nitrogen: IV. a computer simulation, *Mol. Phys.* 30 (3) (1975) 921–949. doi:10.1080/00268977500102461.
- [58] L. Sanguigno, F. Cosentino, D. Larobina, G. Mensitieri, Molecular simulation of carbon dioxide sorption in nanoporous crystalline phase of syndiotactic polystyrene, *Soft Mater.* 9 (2-3) (2011) 169–182. doi:10.1080/1539445x.2011.552360.
- [59] S. Nosé, A unified formulation of the constant temperature molecular dynamics methods, *J. Chem. Phys.* 81 (1) (1984) 511–519. doi:10.1063/1.447334.
- [60] M. Parrinello, A. Rahman, Polymorphic transitions in single crystals: A new molecular dynamics method, *J. Appl. Phys.* 52 (12) (1981) 7182–7190. doi:10.1063/1.328693.
- [61] J.-P. Ryckaert, G. Ciccotti, H. J. C. Berendsen, Numerical integration of the cartesian equations of motion of a system with constraints: Molecular dynamics of *n*-alkanes, *J. Comput. Phys.* 23 (3) (1977) 327–341. doi:10.1016/0021-9991(77)90098-5.
- [62] G. Ciccotti, M. Ferrario, J.-P. Ryckaert, Molecular dynamics of rigid systems in cartesian coordinates A general formulation, *Mol. Phys.* 47 (6) (1982) 1253–1264. doi:10.1080/00268978200100942.
- [63] L. Verlet, Computer “experiments” on classical fluids. I. thermodynamical properties of Lennard-Jones molecules, *Phys. Rev.* 159 (1967) 98–103. doi:10.1103/PhysRev.159.98.

- [64] M. Ferrario, J. Ryckaert, Constant pressure-constant temperature molecular dynamics for rigid and partially rigid molecular systems, *Mol. Phys.* 54 (3) (1985) 587–603. doi:10.1080/00268978500100451.
- [65] B. Widom, Some topics in the theory of fluids, *J. Chem. Phys.* 39 (11) (1963) 2808–2812. doi:10.1063/1.1734110.
- [66] Y. Tamai, H. Tanaka, K. Nakanishi, Molecular simulation of permeation of small penetrants through membranes. 2. solubilities, *Macromolecules* 28 (7) (1995) 2544–2554. doi:10.1021/ma00111a058.
- [67] Y. Tamai, H. Tanaka, K. Nakanishi, Molecular simulation of permeation of small penetrants through membranes. 1. diffusion coefficients, *Macromolecules* 27 (16) (1994) 4498–4508. doi:10.1021/ma00094a011.
- [68] T. Harn (Ed.), *International Tables for Crystallography, Vol. A, Space-Group Symmetry*, Kluwer Academic Publishers, Dordrecht, 2005.
- [69] V. Petraccone, O. Tarallo, V. Califano, Crystal structure of the clathrate form of syndiotactic poly(*m*-methylstyrene) containing carbon disulfide, *Macromolecules* 36 (3) (2003) 685–691. doi:10.1021/ma021313c.
- [70] J. G. Wijmans, R. W. Baker, The solution-diffusion model: A review, *J. Membr. Sci.* 107 (1) (1995) 1–21. doi:10.1016/0376-7388(95)00102-i.
- [71] M. Galizia, C. Daniel, G. Fasano, G. Guerra, G. Mensitieri, Gas sorption and diffusion in amorphous and semicrystalline nanoporous poly(2,6-dimethyl-1,4-phenylene)oxide, *Macromolecules* 45 (2012) 3604–3615. doi:10.1021/ma3000626.
- [72] O. Tarallo, V. Petraccone, C. Daniel, G. Fasano, P. Rizzo, G. Guerra, A chiral co-crystalline form of poly(2,6-dimethyl-1,4-phenylene) oxide (PPO), *J. Mater. Chem.* 22 (23) (2012) 11672–11680. doi:10.1039/c2jm30907f.
- [73] P. Rizzo, G. Ianniello, S. Longo, G. Guerra, Uniplanar orientations and guest exchange in ppo cocrystalline films, *Macromolecules* 46 (2013) 3995–4001. doi:10.1021/ma400313x.
- [74] A. A. Gusev, F. Müller-Plathe, W. F. Van Gunsteren, U. W. Suter, Dynamics of small molecules in bulk polymers, in: *Atomistic Modeling of Physical Properties*, Springer, Berlin, Heidelberg, 1994, pp. 207–247. doi:10.1007/BFb0080200.

- [75] A. A. Gray-Weale, R. H. Henschman, R. G. Gilbert, M. L. Greenfield, D. N. Theodorou, Transition-state theory model for the diffusion coefficients of small penetrants in glassy polymers, *Macromolecules* 30 (1997) 7296–7306. doi:10.1021/ma970349f.
- [76] M. L. Greenfield, Sorption and diffusion of small molecules using transition-state theory, in: *Simulation Methods for Polymers*, CRC Press, Boca Raton, 2004, pp. 409–466. doi:10.1201/9780203021255-20.
- [77] C. Daniel, A. Avallone, P. Rizzo, G. Guerra, Control of crystal size and orientation in polymer films by host-guest interactions, *Macromolecules* 39 (14) (2006) 4820–4823. doi:10.1021/ma0604486.
- [78] J. M. Carr, D. S. Langhe, M. T. Ponting, A. Hiltner, E. Baer, Confined crystallization in polymer nanolayered films: A review, *J. Mater. Res.* 27 (10) (2012) 1326–1350. doi:10.1557/jmr.2012.17.
- [79] J. A. Ibers, W. C. Hamilton (Eds.), *International Tables for X-ray Crystallography, Vol. IV: Revised and Supplementary Tables to Volumes II and III*, Kluwer Academic Publishers, 1989.